


## High performance multifunctional green $\text{Co}_3\text{O}_4$ spinel nanoparticles: photodegradation of textile dye effluents, catalytic hydrogenation of nitro-aromatics and antibacterial potential

S. K. Jesudoss,<sup>a</sup> J. Judith Vijaya,<sup>a</sup> \*<sup>a</sup> P. Iyyappa Rajan,<sup>a</sup> K. Kaviyarasu,<sup>b,c</sup> M. Sivachidambaram,<sup>a</sup> L. John Kennedy,<sup>d</sup> Hamad A. Al-Lohedan,<sup>e</sup> R. Jothiramalingam<sup>e</sup> and Murugan A. Munusamy<sup>f</sup>

Tricobalt tetraoxide ( $\text{Co}_3\text{O}_4$ ), a spinel-structured nanoparticle which possesses mixed oxidation states, has been synthesized via a *Punica granatum* (*P. granatum*, pomegranate) seed extract-mediated green reaction and has been investigated for its superior catalytic activity in three applications, which include (i) photodegradation of textile dye effluents (TDE) collected from the dyeing industry, Tiruppur, Tamil Nadu, India, (ii) catalytic hydrogenation of nitro-aromatic pollutants such as 4-nitrophenol and 4-nitroaniline, and (iii) antibacterial potential in biomedical applications. Prior to the application studies, the synthesized  $\text{Co}_3\text{O}_4$  spinel nanoparticles ( $\text{Co}_3\text{O}_4$ -NPs) were characterized by well-known established techniques such as X-ray diffraction (XRD), high resolution transmission electron microscopy (HRTEM), energy dispersive X-ray analysis (EDX), diffuse reflectance spectroscopy (DRS), photoluminescence spectroscopy (PL), and Raman and FT-IR spectroscopies. We have also discussed the probable mechanism and kinetic studies of the catalytic activity of the  $\text{Co}_3\text{O}_4$ -NPs. Finally, we concluded that the design and development of novel, economic and green synthesis-mediated catalysts such as  $\text{Co}_3\text{O}_4$ -NPs can exhibit efficient catalytic activity in diverse fields, which is necessary for environmental remediation.

Received 9th January 2017,

Accepted 5th March 2017

DOI: 10.1039/c7pp00006e

rsc.li/pps

### 1. Introduction

Transition metal oxides, which have mixed oxidation states, have recently gained significant consideration in cutting edge research because of their unique physical, chemical, electronic and magnetic properties. They have potential applications in technologically important fields, which include but are not limited to drug delivery, artificial cells, waste water treatment,

lightweight fillers, catalysis, supercapacitors, gas sensors, lithium-ion batteries and chemical storage.<sup>1–8</sup> Tricobalt tetraoxide, a spinel-structured material with the molecular formula  $\text{Co}_3\text{O}_4$ , which is sometimes represented as  $\text{CoO}\cdot\text{Co}_2\text{O}_3$ , analogous to  $\text{FeO}\cdot\text{Fe}_2\text{O}_3$ , has rapidly emerged as one of the most popular spinels on account of its novel properties, chemical stability and ease of synthesis in open air atmosphere.<sup>2,9</sup> Furthermore, it represents one of the three cobalt oxide families; the other oxides are rocksalt ( $\text{CoO}$ ) and hexagonal ( $\text{Co}_2\text{O}_3$ ).<sup>10</sup> As is known,  $\text{Co}_3\text{O}_4$  is a p-type semiconducting material;<sup>11</sup> in its spinel structure,  $\text{Co}^{2+}$  ions occupy the tetragonal 8(a) sites,  $\text{Co}^{3+}$  ions occupy the octahedral 16(d) sites and  $\text{O}^{2-}$  ions are located at the 32(e) sites, arranged in a cubic close-packed structure.<sup>1,12</sup> In recent years, researchers have shown great interest in demonstrating the catalytic activity of single and binary metal oxides<sup>13–18</sup> as substitutes for the noble transition metals.  $\text{Co}_3\text{O}_4$  is a transition metal oxide and is less expensive than noble metals; also, it can act as an efficient catalyst in heterogeneous chemical reactions for environmental remediation. In this regard, the interest of our research group was aroused to explore the catalytic activity of  $\text{Co}_3\text{O}_4$ -NPs in diverse reactions, which include photocatalytic degradation, catalytic hydrogenation and biomedical applications.

<sup>a</sup>Catalysis & Nanomaterials Research Laboratory, Department of Chemistry, Loyola College (Autonomous), Chennai 600 034, India. E-mail: jvjvijaya78@gmail.com; Fax: +91-44-28175566; Tel: +91-44-28178200

<sup>b</sup>UNESCO-UNISA Africa Chair in Nanosciences/Nanotechnology Laboratories, College of Graduate Studies, University of South Africa (UNISA), Muckleneuk Ridge, P O Box 392, Pretoria, South Africa

<sup>c</sup>Nanosciences African network (NANOAFNET), Materials Research Group (MRG), iThemba LABS-National Research Foundation (NRF), 1 Old Faure Road, 7129, P O Box 722, Somerset West, Western Cape Province, South Africa

<sup>d</sup>Materials Division, School of Advanced Sciences, Vellore Institute of Technology (VIT) University, Chennai Campus, Chennai 600 127, India

<sup>e</sup>Surfactant Research Chair, Chemistry Department, College of Science, King Saud University, Riyadh 11451, Saudi Arabia

<sup>f</sup>Department of Botany and Microbiology, College of Science, King Saud University, Riyadh 11451, Saudi Arabia

The textile dye effluents (TDE) discharged from the dyeing industries of Tirupur have polluted the non-perennial Noyyal River, a tributary river of the Cauvery River in Tamilnadu, India, in recent decades.<sup>19</sup> The degradation of these effluents, which are released from textile industries and have high chemical oxygen demand (COD),<sup>20</sup> requires immediate attention because effluents from textile industries contain high levels of organic matter and diverse reaction products. When discharged into aquatic ecosystems, the effluents cause the depletion of dissolved oxygen content and have adverse effects on aquatic creatures and mankind.<sup>21</sup> Continuous efforts have been made by textile industries to address this issue by means of various methods, such as hydrolysis in basic medium, chemical processes, membrane filtration, biological treatment, and foam flotation.<sup>22–24</sup> However, the above mentioned methods are known to be inadequate for the complete treatment of highly toxic textile industry effluents, necessitating the search for an efficient method. Nevertheless, advanced oxidation processes, such as heterogeneous photocatalytic degradation, the Fenton method, and photo-Fenton methods have been found to be quite successful in the treatment of textile industry effluents.<sup>25–29</sup> Specifically, heterogeneous photocatalytic degradation has emerged as a cost-effective, eco-friendly and efficient method for the treatment of industrial effluents compared to the abovementioned methods.

Nitro-aromatic compounds, such as 4-nitrophenol and 4-nitroaniline, are classified as organic pollutants and are obtained as by-products in pharmaceutical, agrochemical, textile, paper, dye and other chemical industries.<sup>30,31</sup> However, 4-nitrophenol, upon reduction, will be converted into 4-aminophenol, which is used in the synthesis of analgesic and anti-pyretic drugs and also as a corrosion inhibitor.<sup>31</sup> Therefore, protocols for the catalytic hydrogenation of nitro-aromatic compounds by NaBH<sub>4</sub> have been investigated widely by various research groups and it has been discovered that precious metals such as platinum, palladium, gold and silver nanoparticles can act as efficient catalysts for the reduction reaction.<sup>30–32</sup> However, these noble metal catalysts are highly expensive and should be replaced with inexpensive transition metal catalysts with the same catalytic efficiency. The catalytic hydrogenation of 4-nitrophenol and 4-nitroaniline is a well-known model reaction that can be ideally employed to evaluate the catalytic performance of newly designed catalysts.<sup>30</sup>

In the current work, we synthesized Co<sub>3</sub>O<sub>4</sub>-NPs using *Punica granatum* (*P. granatum*, pomegranate) seed extract and investigated their catalytic activity towards both the photo-degradation of textile dye effluents (TDE) and the catalytic hydrogenation of 4-nitroaromatics. In addition to these applications, the biomedical applications of spinel nanoparticle catalysts have been explored in recent years;<sup>33</sup> in this regard, we also examined the antibacterial potential of the Co<sub>3</sub>O<sub>4</sub>-NPs against two Gram positive (*Staphylococcus aureus* and *Bacillus subtilis*) and two Gram negative bacterial strains (*Pseudomonas aeruginosa* and *Escherichia coli*). In brief, the current report investigates the catalytic activity of a single catalyst, Co<sub>3</sub>O<sub>4</sub>-NPs, in diverse reactions, which include photocatalytic degradation of

TDE, catalytic hydrogenation of 4-nitrophenol and 4-nitroaniline, and antibacterial activity against bacterial strains. Also, *P. granatum* seed extract-mediated green synthesis of Co<sub>3</sub>O<sub>4</sub>-NPs is reported for the first time by our group, and its multi-functional abilities towards catalytic and biomedical applications are described.

## 2. Experimental section

### 2.1. Materials and methods

High-purity cobalt(II) nitrate hexahydrate powder, Co(NO<sub>3</sub>)<sub>2</sub>·6H<sub>2</sub>O (Sigma-Aldrich, purity ≥98%) and glycine, C<sub>2</sub>H<sub>5</sub>NO<sub>2</sub> (Sigma-Aldrich, purity ≥98.5%) are the primary ingredients in the synthesis of the Co<sub>3</sub>O<sub>4</sub>-NPs. For the examination of their antibacterial potential, two microbiological media, Muller Hinton Agar (MHA) and Nutrient Broth (NB), and the commercial antibiotic chloramphenicol were purchased from HiMedia Laboratories (Mumbai, India). Sodium borohydride, NaBH<sub>4</sub> (≥98.0%), 4-nitrophenol (≥99.0%) and 4-nitroaniline (≥99.0%) from Sigma-Aldrich were used for the catalytic reduction. Deionised water was purified through a Millipore system for use throughout the experiments. The remaining chemicals were used without further purification.

### 2.2. Synthesis of Co<sub>3</sub>O<sub>4</sub>-NPs

The hot plate combustion method was employed to synthesize Co<sub>3</sub>O<sub>4</sub>-NPs from an aqueous solution of cobalt(II) nitrate (Co(NO<sub>3</sub>)<sub>2</sub>·6H<sub>2</sub>O), *P. granatum* seed extract (5 mL) and glycine (C<sub>2</sub>H<sub>5</sub>NO<sub>2</sub>). The amount of precursor that needed to be weighed for the synthesis was estimated using the stoichiometric ratio, and 1.5 g of final product was obtained. Initially, the precursors were dissolved in 70 mL of deionised water and maintained for 1 h with continuous stirring to attain a homogenous mixture solution. In the hot plate combustion method, the above homogeneous solution was placed in a hot plate heater (Barnstead Thermolyne, model no: SP46925) and uniformly heated to 250 °C for 15 min; this led to evaporation of the water and combustion of the reaction mixture. The black precipitate was then separated through centrifugation and washed multiple times with deionized water. The separated black powder was dried at 100 °C in a hot air oven and subjected to annealing at 300 °C for 2 h. The hot plate combustion reaction proceeded through an exothermic reduction–oxidation reaction in which the combustion of cobalt(II) nitrate (Co(NO<sub>3</sub>)<sub>2</sub>·6H<sub>2</sub>O) (oxidizing agent) with glycine and *Punica granatum*, which are known to be reducing agents, in stoichiometric quantities ultimately resulted in the formation of Co<sub>3</sub>O<sub>4</sub> NPs.

### 2.3. Analytical methods for catalyst characterization

The Co<sub>3</sub>O<sub>4</sub>-NPs were characterized by the following measurements. X-ray diffraction (XRD) patterns were studied on a Siemens D5000 diffractometer using Cu Kα radiation in continuous scan mode to collect data over the 2θ range of 10° to 90°. Fourier transform infrared (FT-IR) spectra were recorded as KBr pellets with 32 scans per run in the range of 400 to

4000  $\text{cm}^{-1}$  using a Bruker Equinox 55 spectrophotometer. The Raman active modes of the vibrations were observed using a Raman spectrophotometer (STR-250 Seki Technotron Corporation). For the high resolution transmission electron microscopy (HRTEM), a Jeol JEM 4000EX electron microscopy unit with a resolution limit of about 0.12 nm equipped with a Gatan digital camera was employed to image the size and shape of the  $\text{Co}_3\text{O}_4$ -NPs. The chemical composition of the synthesized sample was confirmed by energy dispersive X-ray spectroscopy (EDS) with an Oxford Instruments X Max solid-state silicon drift detector operating at 20 keV. The diffuse reflectance UV-visible spectra of the  $\text{Co}_3\text{O}_4$ -NPs were recorded on a Cary 100 UV-visible spectrophotometer to estimate the energy band gap. In addition, the emission spectra were recorded using a Varian Cary Eclipse fluorescence spectrophotometer at an excitation wavelength of 370 nm.

#### 2.4. Photocatalytic reactor setup and degradation procedure

The photocatalytic degradation (PCD) experiments of textile dye effluents (TDE) collected from the dyeing industry, Tiruppur, Tamil Nadu, India, were performed in a multi lamp photocatalytic reactor. The reactor was equipped with low pressure mercury lamps (8/8 W) which can emit UV radiation; from our trial experiments, we confirmed that a wavelength of 365 nm is adequate for the photocatalytic degradation of TDE. The borosilicate reactor tubes are designed to hold 100 mL of the TDE dye solution. The experimental procedure to perform the PCD reaction is as follows. The initial COD of the TDE was fixed in  $\text{mg L}^{-1}$ , and a known amount of  $\text{Co}_3\text{O}_4$ -NPs were added to this solution and placed in dark conditions for 12 h to attain adsorption equilibrium; the resulting COD was then estimated. The above solution was placed inside the photocatalytic reactor and irradiated with UV light for 2.30 h. Equal aliquots were taken from the reactor tube at regular intervals of 30 min, followed by centrifugation and continuous recording of the UV spectra of the collected samples. The percentage of COD removal was calculated from eqn (1):

$$\% \text{ Removal of COD}(\text{mg L}^{-1}) = \frac{(\text{Initial COD} - \text{Final COD})}{\text{initial COD}} \times 100. \quad (1)$$

According to the recommendation of the Indian Pollution Control Board standard, TDE's discharged from textile dyeing industries into an aquatic ecosystem must contain only  $250 \text{ mg L}^{-1}$  COD;<sup>9</sup> therefore, PCD of the TDE was performed using the  $\text{Co}_3\text{O}_4$ -NPs to decrease the COD to a value below  $250 \text{ mg L}^{-1}$ .

#### 2.5. Analysis of the antibacterial potential of the $\text{Co}_3\text{O}_4$ -NPs

The antibacterial potential of the  $\text{Co}_3\text{O}_4$ -NPs was investigated by the disk diffusion method against Gram-positive and Gram-negative bacterial strains. A total of four bacterial strains, including two Gram-positive bacteria (*Staphylococcus aureus*, *Bacillus subtilis*) and two Gram-negative bacteria (*Pseudomonas aeruginosa*, *Escherichia coli*), were chosen for the investigation of the antibacterial potential of the  $\text{Co}_3\text{O}_4$ -NPs. Bacteria were

sub-cultured from pure cultures of the different strains of bacteria in Nutrient Broth overnight at 37 °C. The turbidity of the bacterial culture was maintained at 0.5 McFarland Standard. Each bacterial strain was swabbed uniformly onto the surface of Mueller–Hinton agar medium in isolated agar plates using sterile cotton swabs in sterile conditions. Sterile paper disks were placed on the agar plates, and 10  $\mu\text{L}$  of 0.001 g/10  $\mu\text{L}$  (w/v) concentrations of  $\text{Co}_3\text{O}_4$ -NPs were applied to the disks. The antibiotic chloramphenicol (10 mcg per disk) was chosen as the standard drug for the determination of the antibacterial potential of the  $\text{Co}_3\text{O}_4$ -NPs. All the strains of bacteria treated with  $\text{Co}_3\text{O}_4$ -NPs and the standard antibiotic chloramphenicol were incubated at 37 °C for 24 h. The antibacterial tests were performed in doublet mode. The zone of inhibition, which appeared as a clear area in the disks, was measured and compared with the standard chloramphenicol.

#### 2.6. Catalytic reduction of 4-nitrophenol and 4-nitroaniline

An ice cold aqueous solution of sodium borohydride (1 mL) was added to 4-nitrophenol (1.7 mL) in a standard quartz cuvette. The light yellow colour of the 4-nitrophenol gradually changed to yellowish green due to the formation of 4-nitrophenolate ion. Then, a known amount of  $\text{Co}_3\text{O}_4$ -NPs (0.02 g) synthesized by the hot plate combustion method was added to the above solution, and time-dependent UV-visible absorbance spectra were continuously monitored for the resulting solution at regular intervals of 30 s. The same experimental procedure was followed for the catalytic reduction using 4-nitroaniline.

## 3. Results and discussion

### 3.1. Structural properties of the $\text{Co}_3\text{O}_4$ -NPs

The X-ray diffractogram (XRD) of the as-synthesized  $\text{Co}_3\text{O}_4$ -NPs is reported in Fig. 1; it is evident that this diffractogram shows very well defined peaks, indicating the presence of a highly crystalline phase. The X-ray diffractogram was indexed with

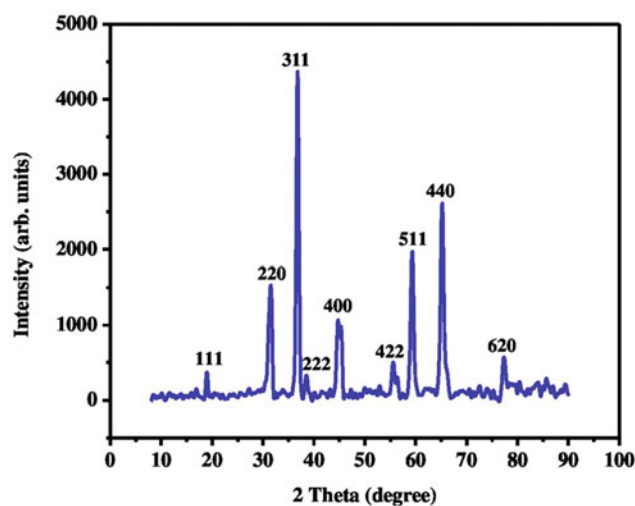


Fig. 1 X-ray diffraction (XRD) pattern of the  $\text{Co}_3\text{O}_4$ -NPs.

JCPDS card number 65-3103, and the peaks were indexed with the face-centered cubic spinel structure with the space group of  $Fd3m$ . The major Bragg reflections were noted as peaks at  $2\theta$  values of about  $19.06^\circ$ ,  $31.33^\circ$ ,  $36.84^\circ$ ,  $38.71^\circ$ ,  $44.88^\circ$ ,  $55.77^\circ$ ,  $59.60^\circ$ ,  $65.55^\circ$ , and  $77.55^\circ$ , which are assigned to the (111), (220), (311), (222), (400), (422), (511), (440) and (620) lattice planes respectively, which also matched significantly well with the above mentioned JCPDS card number; we omitted the indexing of the much lower intensity peaks observed in Fig. 1. The occurrence of very high intensity peaks in Fig. 1 reveals the highly crystalline nature of the  $\text{Co}_3\text{O}_4$ -NPs; furthermore, no additional peaks exist in the diffractogram, which confirms the absence of impurity phases and ultimately endorses the purity of the  $\text{Co}_3\text{O}_4$  phase.

The chemical bonding information in the  $\text{Co}_3\text{O}_4$ -NPs was evaluated using Fourier transform infrared spectroscopy (FT-IR) at room temperature; the characteristic IR bands were plotted in the range of  $4000$  to  $500\text{ cm}^{-1}$ , as displayed in Fig. 2a. Furthermore, this analysis provides significant information about the presence of anions intercalated between the  $\text{Co}_3\text{O}_4$ -NPs.<sup>34,35</sup> The OH stretching and bending vibrations are represented by a broad band centered at  $3416\text{ cm}^{-1}$  and a sharp band at  $1635\text{ cm}^{-1}$ , which confirm that atmospheric water molecules are absorbed in the  $\text{Co}_3\text{O}_4$ -NPs.<sup>35,36</sup> A broad IR band appearing around  $1405\text{ cm}^{-1}$  was assigned to the asymmetric stretching of perturbed intercalated carbonate anions ( $\text{CO}_3^{2-}$ ) with  $C_{2v}$  symmetry, which emerges due to the stronger electrostatic interactions between  $\text{Co}^{2+}$  and  $\text{CO}_3^{2-}$  ions and hence causes a certain extent of perturbation (free  $\text{CO}_3^{2-}$  should have a peak at  $1415\text{ cm}^{-1}$ ).<sup>34,35</sup> Another IR band at  $1072\text{ cm}^{-1}$  was assigned to the symmetric stretching of  $\text{CO}_3^{2-}$  ion. In addition, two well-defined, sharp IR bands at  $667$  and  $570\text{ cm}^{-1}$  are attributable to the fingerprint stretching vibrational modes of cobalt–oxygen (Co–O) bonds, thus confirming the formation of the  $\text{Co}_3\text{O}_4$ -NPs.<sup>34–36</sup> In particular, the band at  $570\text{ cm}^{-1}$  is characteristic of Co–O bonding vibrations and represents the presence of  $\text{Co}^{3+}$  ions in the octahedral site. However, the band at  $667\text{ cm}^{-1}$  denotes  $\text{ABO}_3$ -type  $\text{Co}^{2+}$ – $\text{Co}^{3+}$ – $\text{O}_3$  bonding vibrations (where A denotes the  $\text{Co}^{2+}$  in the tetrahedral site) of the crystal lattice of the spinel structure.

For additional validation of the vibrational frequencies, the Raman spectrum was measured for the synthesized  $\text{Co}_3\text{O}_4$ -NPs, which are in a spinel configuration with the space group " $Fd3m$ ".<sup>36</sup> The active modes of " $Fd3m$ " are given as follows.

$$\Gamma = A_{1g}(\text{R}) + E_g(\text{R}) + F_{1g}(\text{IN}) + 3F_{2g}(\text{R}) + 2A_{2u}(\text{IN}) + 2E_u(\text{IN}) + 4F_{1u}(\text{IR}) + 2F_{2u}(\text{IN}) \quad (2)$$

where (R), (IR), and (IN) are the Raman active, infrared active and inactive modes of vibrations. From eqn (2), one can expect five Raman active modes, which are specified as the  $A_{1g}$ ,  $E_g$  and  $3F_{2g}$  modes of vibrations. The Raman spectrum of the  $\text{Co}_3\text{O}_4$ -NPs is shown in Fig. 2b; we can observe five Raman bands at  $195$ ,  $475$ ,  $515$ ,  $612$ , and  $685\text{ cm}^{-1}$ , respectively. The band at  $685\text{ cm}^{-1}$  is a characteristic band of the  $A_{1g}$  mode, and the bands centered at  $195$ ,  $515$ , and  $612\text{ cm}^{-1}$  are assigned to the  $3F_{2g}$  mode.<sup>37</sup> The  $E_g$  mode of vibration is observed at  $475\text{ cm}^{-1}$ .<sup>37</sup> The shift in the observed Raman bands in our samples from the reference may be due to the existence of size effects or surface stress/strain.<sup>36</sup>

### 3.2. Morphological characteristics of the $\text{Co}_3\text{O}_4$ -NPs

Further insight into the nanostructured  $\text{Co}_3\text{O}_4$ -NPs was obtained by typical observations made at various magnification ranges using high resolution transmission electron microscopy (HRTEM) analysis. As shown in Fig. 3(a–h), in various scales of magnification, the  $\text{Co}_3\text{O}_4$ -NPs possess nearly quasi-spherical shapes with high agglomeration. The likely explanation behind this high agglomeration is the association of spinel nanoparticles in the highly concentrated sample during the sample processing in HRTEM analysis;<sup>38</sup> it may also be due to the stronger electrostatic interactions between  $\text{Co}^{2+}$  and  $\text{CO}_3^{2-}$  ions *via* intercalation in the crystal lattice layers of the  $\text{Co}_3\text{O}_4$  NPs. The inset histogram in Fig. 3e depicts the total number of particle counts of various sizes of nanoparticles in the range from  $1$  to  $7\text{ nm}$ ; the maximum of the particle counts is located in the particle size range of  $3.5\text{ nm}$ . The selective area electron diffraction (SAED) analysis is shown in Fig. 3h; it confirms the polycrystalline nature of the  $\text{Co}_3\text{O}_4$ -NPs. This pattern was obtained due to the successive reflec-

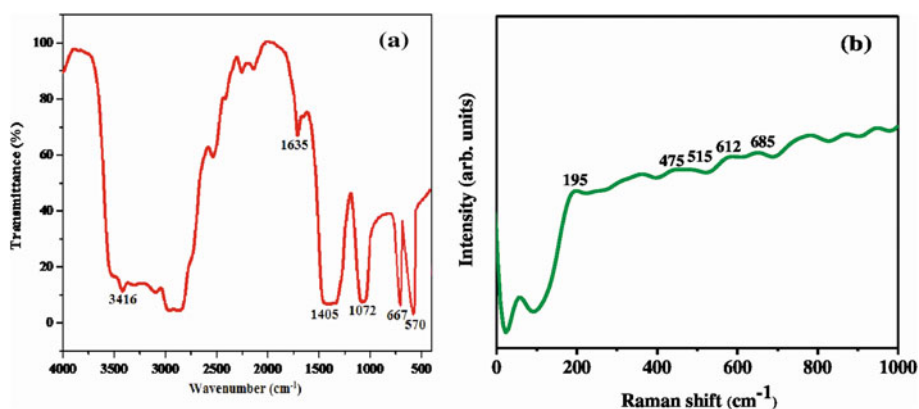
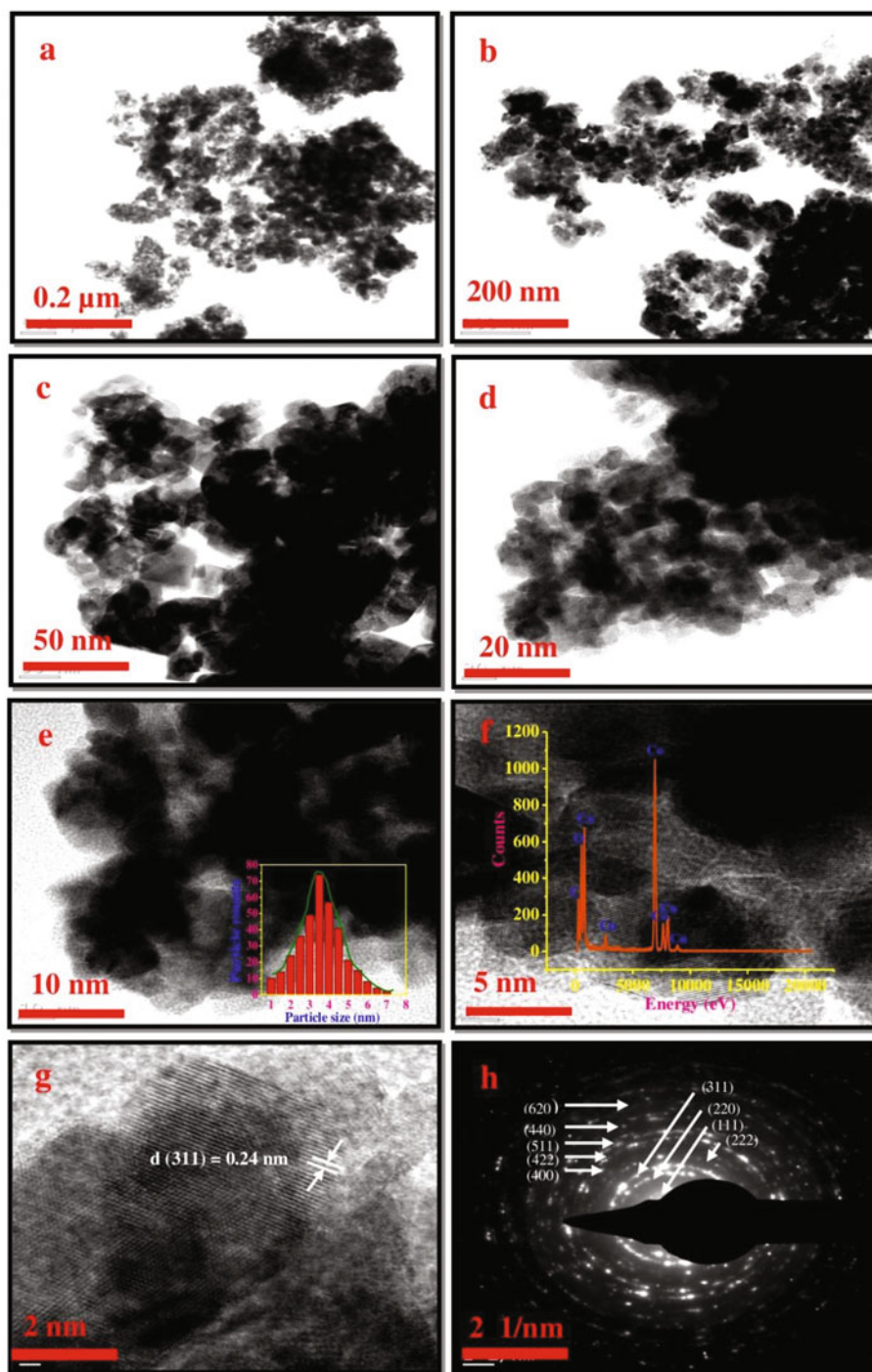


Fig. 2 (a) Fourier transform infrared (FT-IR) spectrum and (b) Raman spectrum of the  $\text{Co}_3\text{O}_4$ -NPs.





**Fig. 3** (a–h) HRTEM images with different scales of magnification, particle size distribution of the histogram model (inset 3e), energy dispersive X-ray (EDX) spectrum (inset 3f) and SAED pattern (inset 3h) of the  $\text{Co}_3\text{O}_4$ -NPs.

tions correlated to the (111), (220), (311), (222), (400), (422), (511), (440), and (620) lattice planes, which is in good agreement with our XRD results. The fringe spacing corresponding to the (311) lattice plane was measured to be 0.24 nm, which is in good agreement with the values reported in other experimental works.<sup>39,40</sup> The elemental composition analysis and the chemical purity of the  $\text{Co}_3\text{O}_4$ -NPs were characterized from

the energy dispersive X-ray (EDX) spectrum, as shown in Fig. 3f. The peaks of the respective cobalt and oxygen atoms are clearly visible from the EDX spectrum and affirm the very high purity of the product. In addition to these peaks, the noticeable peaks of carbon and copper atoms arose from the carbon coated copper grid sample holder during the course of sampling.

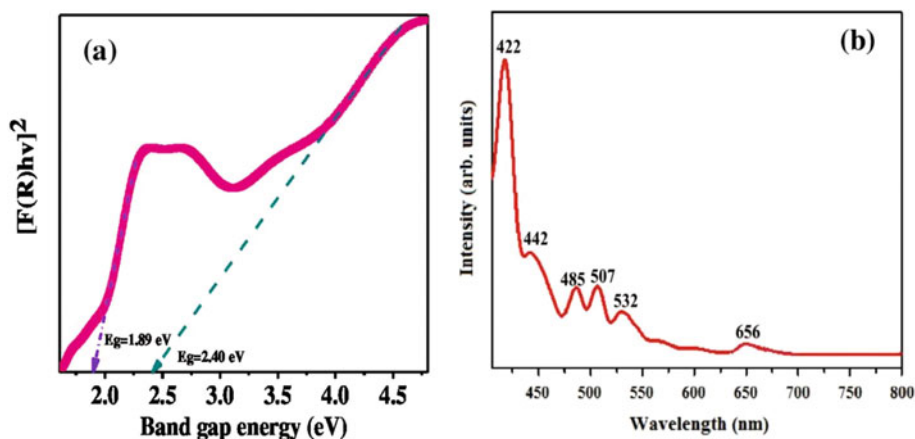


Fig. 4 (a) UV-Vis reflectance spectrum and (b) PL spectrum of the  $\text{Co}_3\text{O}_4$ -NPs.

### 3.3. Optical properties of the $\text{Co}_3\text{O}_4$ -NPs

The optical properties of nano-sized materials can vary according to their structures and morphologies, which usually differ from those of the bulk materials. As mentioned earlier,  $\text{Co}_3\text{O}_4$  is a p-type semiconducting material; its optical band gaps were estimated from the UV-Visible diffuse reflectance spectrum (DRS). The Kubelka–Munk (K–M) function model was followed to calculate the optical band gaps of the  $\text{Co}_3\text{O}_4$ -NPs. The expression of the K–M model is as follows:<sup>33</sup>

$$\alpha = F(R) = \frac{(1 - R)^2}{2R} \quad (3)$$

where  $\alpha$  is the linear absorption coefficient,  $R$  is the reflectance and  $F(R)$  is the Kubelka–Munk function. The Tauc relation is expressed as follows:<sup>33</sup>

$$F(R)h\nu = A(h\nu - E_g)^n \quad (4)$$

The values  $n = 2$  and  $n = 1/2$  represent indirect and direct band gaps, respectively. The Tauc plot of  $[F(R)h\nu]^2$  against the band gap energy (eV) was plotted and is shown in Fig. 4a; two linear relationship regions were observed. The first region is in the range between 2.00 and 2.28 eV, which gives a band gap value of 1.89 eV and is assigned to the  $\text{O}^{2-}$ – $\text{Co}^{2+}$  charge transfer process (excitation from the valence to the conduction band).<sup>41</sup> The other region was observed in the range between 3.94 and 4.45 eV, which gives a band gap value of 2.40 eV and is assigned to the  $\text{O}^{2-}$ – $\text{Co}^{3+}$  charge transfer process (where  $\text{Co}^{3+}$  ions occupy the region below the conduction band).<sup>41,42</sup>

Photoluminescence emission spectra can provide valuable information about the intrinsic and extrinsic defects in the crystal lattices of nanoparticles; the room temperature emission spectrum of the  $\text{Co}_3\text{O}_4$ -NPs with an excitation wavelength of 370 nm is shown in Fig. 4b. In Fig. 4b, the emission peaks originating at 422, 442, 485, 507, 532, and 656 nm for the  $\text{Co}_3\text{O}_4$ -NPs in the visible region are due to the radiative recombination of photo-generated holes; this recombination process occurs due to minor structural defects, such as oxygen vacancies and cobalt ions occupying interstitial positions.

### 3.4. Photocatalytic activity of $\text{Co}_3\text{O}_4$ -NPs in the degradation of textile dye waste effluents (TDE)

Prior to the photodegradation experiments, a pilot reaction was performed in order to substantiate the photocatalytic ability of the  $\text{Co}_3\text{O}_4$ -NPs, which was in turn evaluated from the COD removal efficiency of TDE under UV light irradiation. The decrease in the COD level and the disappearance of color affirms the destruction of the organic compounds in TDE. The photocatalytic activity of the  $\text{Co}_3\text{O}_4$ -NPs in the degradation of TDE was examined by continuous monitoring of the absorbance intensity of TDE by UV-visible spectrophotometry, and the COD removal efficiency was found to be influenced by two experimental operating parameters: the catalyst loading and the pH of the medium. The COD removal from TDE with an initial concentration fixed at  $750 \text{ mg L}^{-1}$  was investigated using various amounts of  $\text{Co}_3\text{O}_4$ -NP loading, as shown in Fig. 5a. The results show an evident linear increase in the COD removal efficiency with increasing catalyst dosage up to the optimum level of 50 mg of catalyst. Further increases in the catalyst dosage decreased the COD removal efficiency; this is not shown in Fig. 5a. The likely explanation behind this observation is that as the catalyst dosage increases, the formation of active sites on the catalyst surface increases, which in turn produces more hydroxyl radicals ( $\cdot\text{OH}$ ) and superoxide radical ions ( $\cdot\text{O}_2^-$ ).<sup>33</sup> However, a further increase in the catalyst dosage will result in the agglomeration of nanoparticles and block the UV light illumination on the surface of the  $\text{Co}_3\text{O}_4$  photocatalyst, which can inhibit the production of ( $\cdot\text{OH}$ ) radical, a primary oxidant in COD experiments.<sup>33</sup> Next, we investigated the effect of pH on the COD removal of TDE with the optimum dosage of catalyst (50 mg). The pH of the reaction medium plays an essential role in the COD removal process because it influences the rate of production of hydroxyl radicals ( $\cdot\text{OH}$ ), a powerful oxidizing agent in the photodegradation reaction. To investigate this effect, photodegradation experiments were performed in the pH range of 2 to 12, and the effects on the COD removal efficiency are displayed in Fig. 5b. The maximum COD removal efficiency of 98.9% was observed at the highly acidic

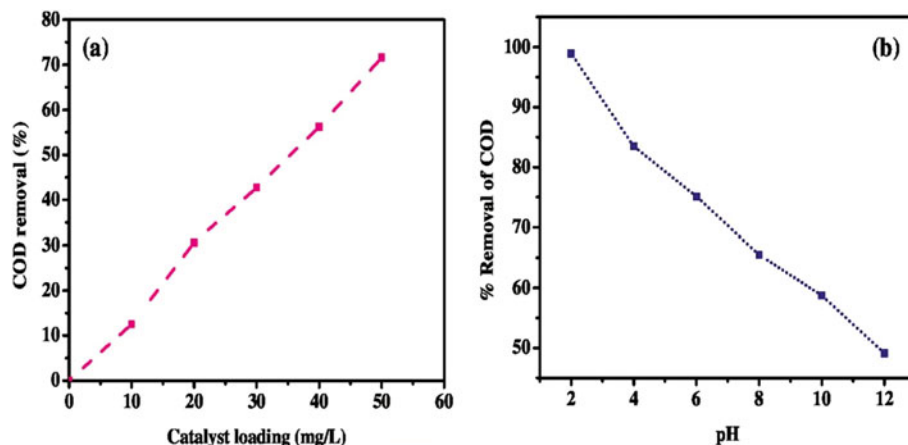


Fig. 5 The PCD of TDE in the presence of  $\text{Co}_3\text{O}_4$ -NPs: (a) effect of the catalyst loading; (b) effect of pH (experimental conditions: initial concentration of TDE =  $750 \text{ mg L}^{-1}$  of COD,  $t = 150 \text{ min}$ ,  $\lambda = 365 \text{ nm}$ ).

pH of 2; however, it decreased when the pH of the reaction medium was increased and reached only 49.1% at pH 12. Based upon these results, we fixed pH 2 as the optimum level for further photodegradation experiments. The point of zero charge ( $\text{pH}_{\text{ZPC}}$ ) of  $\text{Co}_3\text{O}_4$  is 7.3; thus, the surface of the  $\text{Co}_3\text{O}_4$  photocatalyst holds a net positive charge when the pH of the solution is below  $\text{pH}_{\text{ZPC}}$  ( $\text{pH} < \text{pH}_{\text{ZPC}}$ ) and efficiently accelerates the adsorption of negatively charged TDE molecules on the surface of the  $\text{Co}_3\text{O}_4$  photocatalyst.<sup>20,43,44</sup> Likewise, when the medium becomes basic ( $\text{pH} > \text{pH}_{\text{ZPC}}$ ), hydroxide ( $\text{OH}^-$ ) ions are preferentially adsorbed on the  $\text{Co}_3\text{O}_4$  photocatalyst surface.<sup>20,44</sup> As a result, ion-dipole repulsive forces originate between the negatively charged photocatalyst surface and the negatively charged TDE molecules that are expected at pH values higher than the  $\text{pH}_{\text{ZPC}}$ .<sup>20,21,44</sup> Hence, TDE shows a lower rate of photocatalytic degradation at higher alkalinity. Also, the higher concentration of  $\text{OH}^-$  ions in the reaction medium prevents the penetration of UV light to the surface of the  $\text{Co}_3\text{O}_4$  photocatalyst. Moreover, alkaline pH medium favors the production of carbonate ions, which are considered to be effective scavengers of  $\text{OH}^-$  ions; this leads to a decrease in the rate of COD removal.<sup>21</sup> The factors responsible for the

higher rate of photocatalytic degradation at lower pH values can be explained as follows. The positive holes ( $\text{h}^+$ ) are the major oxidation species at lower pH. The lower pH generates more  $\text{H}^+$  ions that are adsorbed on the surface of  $\text{Co}_3\text{O}_4$  photocatalyst; thus, the catalyst surface is positively charged.<sup>44</sup> These positively charged  $\text{Co}_3\text{O}_4$ -NPs support the excitation of photo-induced electrons, which react with the adsorbed  $\text{O}_2$  molecules to produce superoxide radical anions ( $^{\bullet}\text{O}_2^-$ ) ( $\text{O}_2 + \text{e}^- \rightarrow ^{\bullet}\text{O}_2^-$ ).<sup>20,21,44</sup> Also, the positively charged  $\text{Co}_3\text{O}_4$ -NPs restrict the recombination of excited electrons and positive holes and produce more hydroxyl radicals ( $^{\bullet}\text{OH}$ ) by the reaction between the positive holes and water molecules.<sup>21</sup> Both the radical ions  $^{\bullet}\text{O}_2^-$  and  $^{\bullet}\text{OH}$  have been proved to be strong oxidants and are responsible for the enhanced photodegradation of TDE.

Kinetic studies of the photocatalytic degradation of TDE using the  $\text{Co}_3\text{O}_4$ -NPs were also performed by employing the optimized parameters of  $t = 150 \text{ min}$ , initial concentration =  $750 \text{ mg L}^{-1}$  COD, photocatalyst dosage =  $50 \text{ mg}$ , light intensity =  $365 \text{ nm}$  and  $\text{pH} = 2$ . Fig. 6a shows the extent of COD removal ( $\text{mg L}^{-1}$ ) with respect to time (min) in the presence of  $\text{Co}_3\text{O}_4$ -NPs during the PCD reaction; the COD removal efficiency of the  $\text{Co}_3\text{O}_4$ -NPs in the degradation of TDE was calculated to be

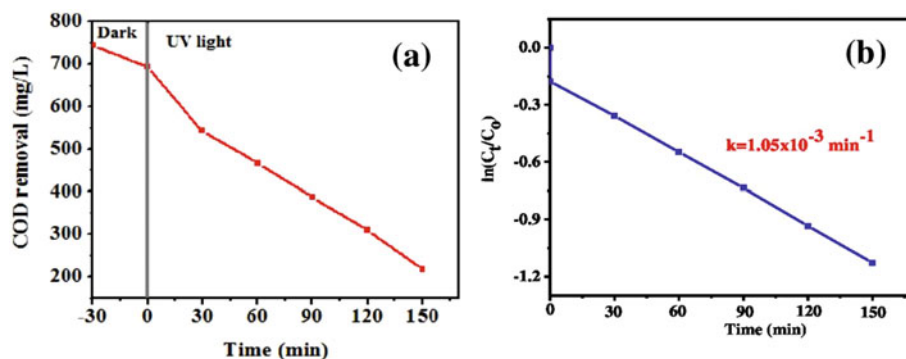


Fig. 6 The PCD of TDE in the presence of  $\text{Co}_3\text{O}_4$ -NPs: (a) effect of time; (b) kinetic plot of  $\ln(C_t/C_0)$  versus reaction time ( $t$ , min) (experimental conditions: initial concentration of TDE =  $750 \text{ mg L}^{-1}$  of COD, catalyst loading =  $50 \text{ mg}$ ,  $\lambda = 365 \text{ nm}$ ).

70.69% after 150 min. The PCD reaction was stopped at 150 min because at this specific time, the concentration level of COD in TDE was found to be below 250 mg L<sup>-1</sup> (as per the standards of the Indian Pollution Control Board for industrial waste water discharged into river bodies). This reaction can be expressed as pseudo first-order kinetics by eqn (5):

$$\ln(C_t/C_0) = -k_1 t \quad (5)$$

where  $k$  is the pseudo first-order rate constant (min<sup>-1</sup>),  $C_0$  is the initial concentration of TDW (750 mg L<sup>-1</sup>) and  $C_t$  is the concentration of TDW at reaction time  $t$  (min). A pseudo first-order

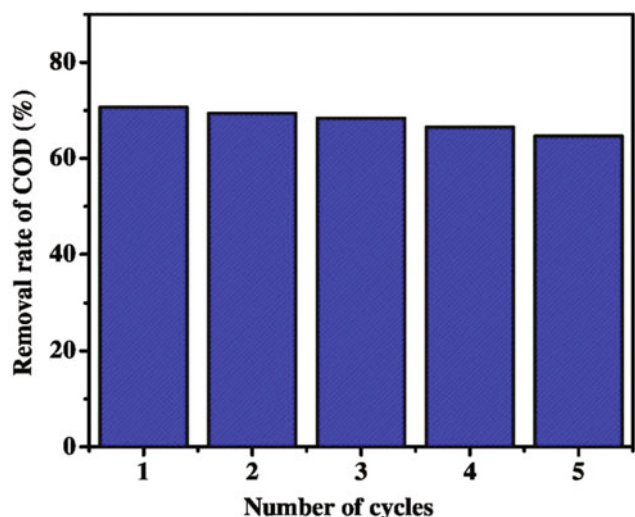
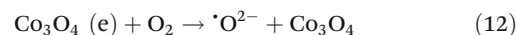
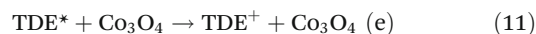
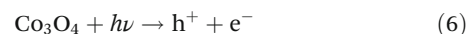


Fig. 7 Reusability studies of the PCD of TDE in the presence of Co<sub>3</sub>O<sub>4</sub>-NPs (experimental conditions: initial concentration of TDE = 750 mg L<sup>-1</sup> of COD, catalyst loading = 50 mg,  $t$  = 150 min,  $\lambda$  = 365 nm).

rate constant value of  $1.05 \times 10^{-3} \text{ min}^{-1}$  and a regression correlation coefficient ( $R^2$ ) value of 0.9997 were obtained from the slope of the linear plot of  $\ln(C_t/C_0)$  versus irradiation time, as shown in Fig. 6b. The significant value of  $R^2$  (0.9997) confirms that the PCD reaction follows pseudo first-order kinetics. Reusability experiments of the Co<sub>3</sub>O<sub>4</sub>-NPs as a photocatalyst in the degradation of TDE were performed for five successive cycles, and the removal rates of COD (%) are shown in Fig. 7. These reusability results imply excellent COD removal efficiency of the Co<sub>3</sub>O<sub>4</sub>-NPs even after five successive cycles of PCD experiments. The probable degradation mechanism for TDE using the Co<sub>3</sub>O<sub>4</sub>-NPs is given below and is also shown in Fig. 8.



In the above mechanism, the first three steps ((6), (7), and (8)) involve the formation of active species for the PCD reaction, such as  $\text{O}_2^{\bullet-}$  and  $\text{OH}^\bullet$  radical ions, due to the illumination of UV light on the surface of the Co<sub>3</sub>O<sub>4</sub>-NPs; the TDE degradation takes place in step (9). Steps (10), (11), and (12) account for the sensitization of TDE molecules under the illumination of UV light; this process enables insertion of the electrons into the crystal lattice of the Co<sub>3</sub>O<sub>4</sub>-NPs,

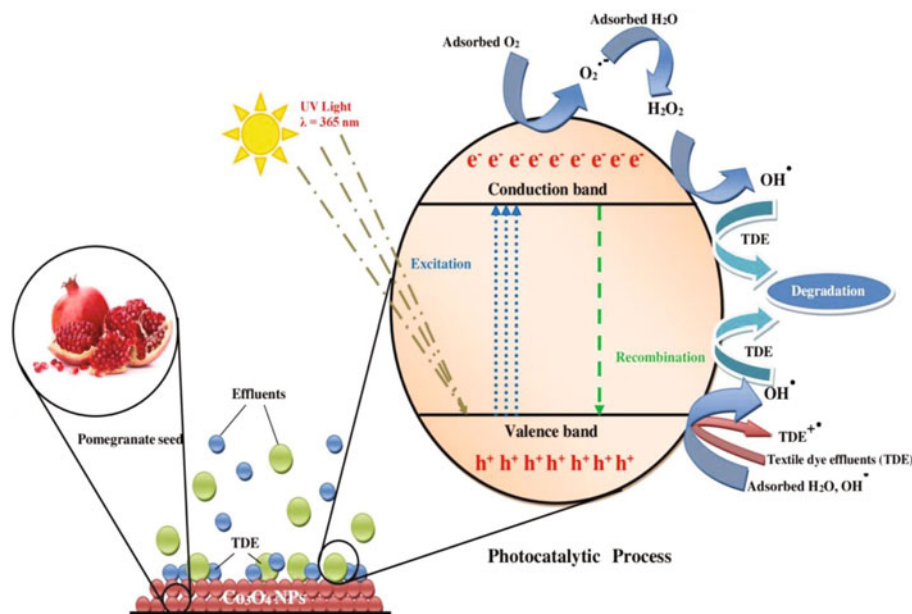


Fig. 8 Photocatalytic degradation mechanism of TDE using the Co<sub>3</sub>O<sub>4</sub>-NPs.



which ultimately leads to the formation of  $\cdot\text{O}_2^-$  ions upon reaction with  $\text{O}_2$  molecules and would be utilized in the PCD reaction.

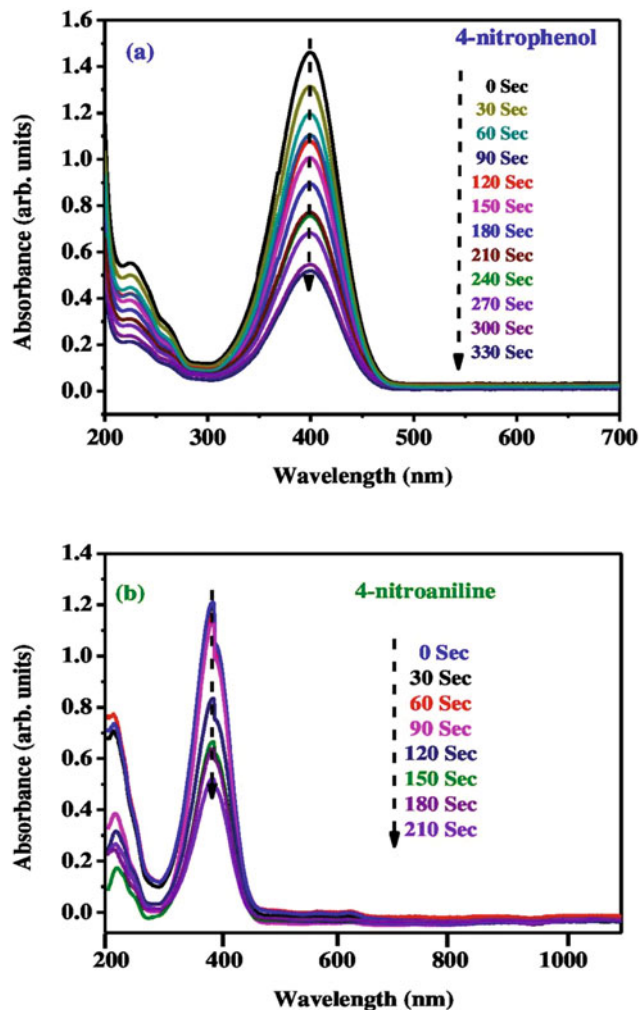


Fig. 9 Time course profile showing the catalytic reductions of (a) 4-nitrophenol and (b) 4-nitroaniline using the  $\text{Co}_3\text{O}_4$ -NPs.

### 3.5. Catalytic and kinetic studies of the $\text{Co}_3\text{O}_4$ -NPs in the reduction of 4-nitrophenol and 4-nitroaniline

The catalytic activity of the  $\text{Co}_3\text{O}_4$ -NPs was evaluated by performing one of the most frequently used, typical reactions: the catalytic hydrogenation of 4-nitrophenol and 4-nitroaniline by sodium borohydride. Samples were collected at regular time intervals during the course of reaction, and their UV-visible spectra were monitored continuously. A strong and highly intense absorption peak around 400 nm was initially noticed; this is due to the 4-nitrophenolate ions present in the reaction mixture. However, a significant decrease in the intensity of absorption was clearly visible within 330 s, as shown in Fig. 9a. This observation confirms the conversion of nitro groups into amine groups in the presence of the  $\text{Co}_3\text{O}_4$  spinel nanoparticles. The absence of other absorption peaks in Fig. 9(a and b) confirms that there is no occurrence of side reactions and by-products. An analogous trend was also observed for the hydrogenation of 4-nitroaniline, with a significant decrease in the intensity of the absorption peak at 394 nm within 210 s, as shown in Fig. 9b. Both reactions were carried out at room temperature under mild conditions. An aqueous solution was chosen as the solvent medium. These reactions can be expressed by the pseudo first-order kinetics model (eqn (5)); for the catalytic hydrogenation of 4-nitrophenol, a pseudo first-order rate constant of  $0.32 \times 10^{-2} \text{ s}^{-1}$  and a regression correlation coefficient ( $R^2$ ) value of 0.9999 were obtained from the slope of the linear plot of  $\ln(C_t/C_0)$  versus the reaction time in minutes, as shown in Fig. 10a. Similarly, the pseudo first-order rate constant for the catalytic hydrogenation of 4-nitroaniline was calculated to be  $1.23 \times 10^{-2} \text{ s}^{-1}$ , and a regression correlation coefficient ( $R^2$ ) value of 0.9992 was obtained from Fig. 10b. The catalytic hydrogenation mechanism is illustrated in Fig. 11; it explores the efficient catalytic activity of the  $\text{Co}_3\text{O}_4$ -NPs for the treatment of industrial effluents containing nitro-aromatics. Moreover, the toxic nature of  $\text{NaBH}_4$  was reduced to a greater extent because the reaction mechanism finally results in the production of a very low toxic compound, sodium metaborate ( $\text{NaBO}_2$ ).

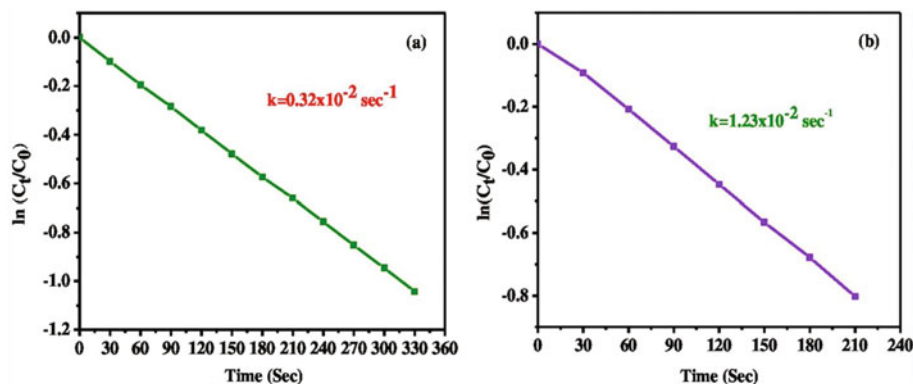


Fig. 10 Pseudo first-order kinetic model for the catalytic hydrogenation of (a) 4-nitrophenol and (b) 4-nitroaniline using the  $\text{Co}_3\text{O}_4$ -NPs.

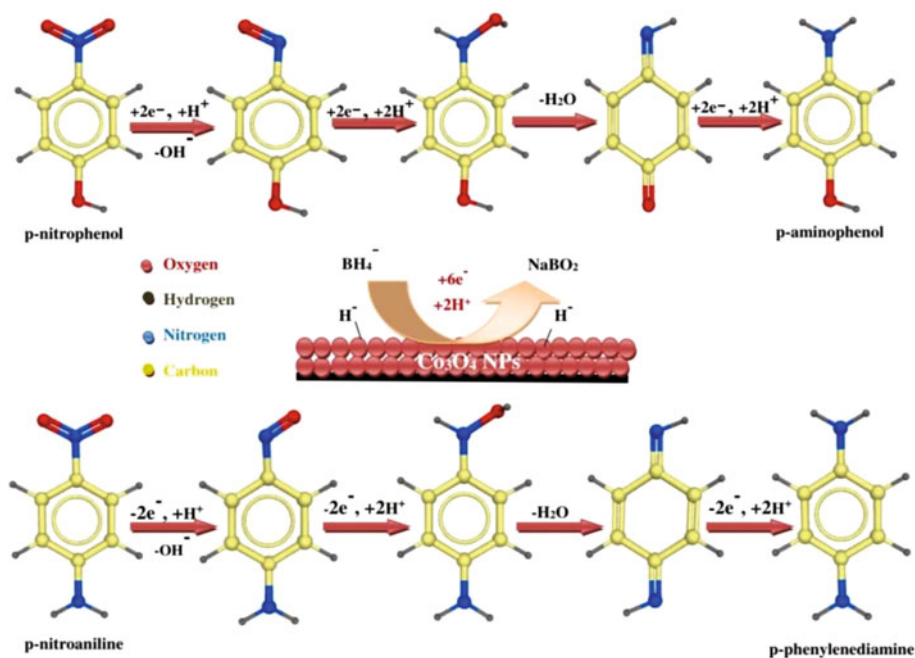


Fig. 11 Catalytic hydrogenation mechanism using the  $\text{Co}_3\text{O}_4$ -NPs.

### 3.6. Analysis of the antibacterial potential of the $\text{Co}_3\text{O}_4$ -NPs

It has been amply established that mixed metal oxides with nanodimensions demonstrate antibacterial effects towards Gram positive and Gram negative bacterial strains.<sup>33,45,46</sup> The as-synthesized  $\text{Co}_3\text{O}_4$ -NPs were evaluated for their antibacterial potential against both Gram positive and Gram negative bacterial strains. Two Gram positive (*Staphylococcus aureus* and *Bacillus subtilis*) and two Gram negative (*Pseudomonas aeruginosa* and *Escherichia coli*) bacterial strains were chosen for this evaluation. Chloramphenicol (10 mcg) was utilized as a standard in order to compare the results of bacterial inhibition with those of the  $\text{Co}_3\text{O}_4$ -NPs. The zone of inhibition (mm) values against the both Gram positive and Gram negative bacterial strains for the  $\text{Co}_3\text{O}_4$ -NPs and the standard chloramphenicol are listed in Table 1, and the inhibitory effects of the  $\text{Co}_3\text{O}_4$ -NPs in comparison with the standard chloramphenicol are plotted in Fig. 12. Our antibacterial activity experiments established that the  $\text{Co}_3\text{O}_4$ -NPs display excellent antagonistic effects on both Gram positive and Gram negative bacterial strains compared to the standard chloramphenicol; the

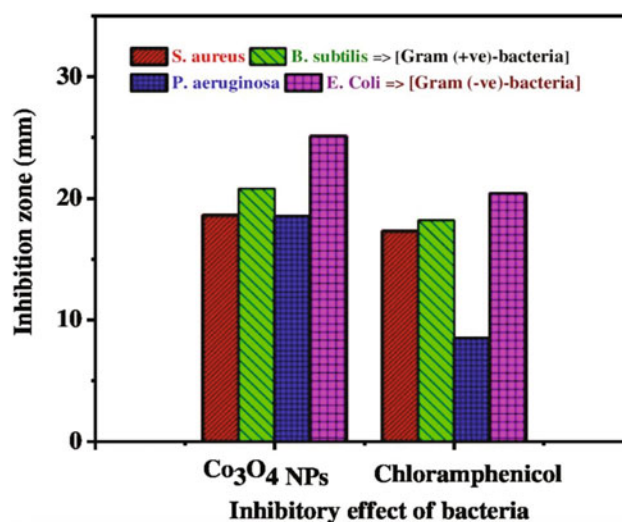


Fig. 12 Inhibitory effects of the  $\text{Co}_3\text{O}_4$ -NPs and the standard chloramphenicol towards bacterial strains.

Table 1 Antibacterial activities of the  $\text{Co}_3\text{O}_4$ -NPs compared to the standard antibiotic chloramphenicol

Bacteria	Zone of inhibition (mm)	
	$\text{Co}_3\text{O}_4$	Chloramphenicol
<i>Staphylococcus aureus</i>	18.6	17.3
<i>Bacillus subtilis</i>	20.8	18.2
<i>Pseudomonas aeruginosa</i>	18.5	8.5
<i>Escherichia coli</i>	25.1	20.4

respective diameters of the inhibition zones in the bacterial strains due to the antibacterial potential of the  $\text{Co}_3\text{O}_4$ -NPs and chloramphenicol are shown in Fig. 13. The differences in the susceptibilities of the different bacterial strains are due to the differences in their oxidative stress tolerance. The antibacterial potential mainly depends upon the particle size, specific surface area and morphology of the spinel nanoparticles; the mechanistic pathway for the inhibiting action of nanoparticles is still ambiguous. A few experimental studies have reported that this antibacterial potential is the result of electrostatic

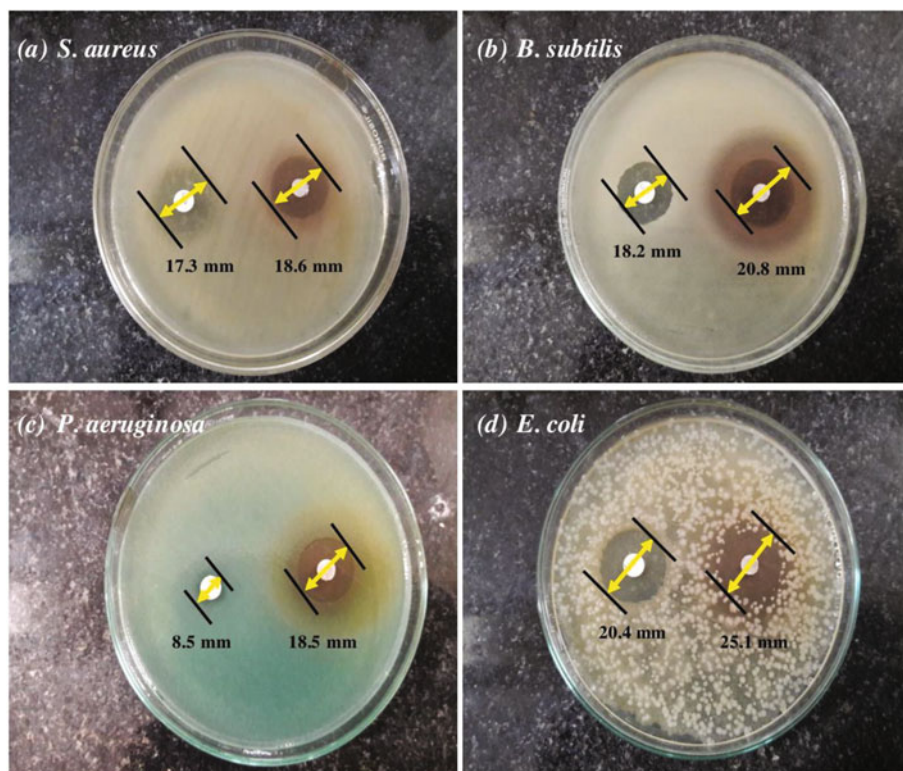


Fig. 13 Zones of inhibition produced by the  $\text{Co}_3\text{O}_4$ -NPs against the bacterial strains (a) *Staphylococcus aureus*, (b) *Bacillus subtilis*, (c) *Pseudomonas aeruginosa* and (d) *Escherichia coli*.

interactions between the bacterial cells and the nanoparticles, which are capable of generating reactive oxygen species (ROS), a factor responsible for bacterial cell destruction.<sup>33,47–50</sup> From this point of view, two probable mechanistic pathways can be suggested, as shown in Fig. 14(a and b).<sup>33</sup> In the first pathway, cobalt ions with different positive oxidation states ( $\text{Co}^{2+}$ ,  $\text{Co}^{3+}$ ) in the  $\text{Co}_3\text{O}_4$ -NPs can experience strong interactions with the negative parts of the bacterial cells, leading to the destruction of the bacterial cells. The other possible pathway occurs due to the irradiation of light on the surface of the spinel nanoparticles, which can lead to the formation of excited electrons

in the conduction band and positive holes in the valence band. The excited electrons in the conduction band react with oxygen molecules to yield superoxide radical anions ( $\text{O}_2^{\cdot-}$ ) followed by the generation of hydrogen peroxide, a strong oxidizing agent. Upon further reaction of the superoxide radical anions with water on the surface of the spinel nanoparticles, the bacteria are destroyed completely. Simultaneously, the positive holes in the valence band can react with water and produce hydroxyl radicals ( $\cdot\text{OH}$ ). Although the hydroxyl radicals and superoxide radical ions cannot penetrate inside cell membranes, they remain in contact with the outer layer of the

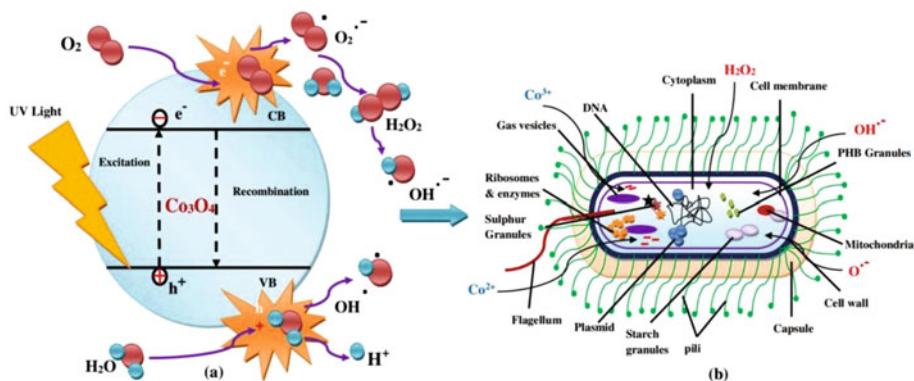


Fig. 14 Schematics of (a)  $\cdot\text{OH}$  formation by light irradiation, (b) inhibition activity of bacterial growth using  $\text{Co}_3\text{O}_4$ -NPs.



bacterial cells and break down proteins and lipids. Thus, the antibacterial potential of the  $\text{Co}_3\text{O}_4$ -NPs at nano-range concentrations shows greater effects for the destruction of microbial organisms.

## 4. Conclusions

$\text{Co}_3\text{O}_4$ -NPs were synthesized *via* a simple, cost-effective *Punica granatum* (*P. granatum*, pomegranate) seed extract-mediated green reaction the using hot plate combustion method and were well characterized. The synthesized  $\text{Co}_3\text{O}_4$ -NPs show a highly crystalline phase and possess quasi-spherical shapes with high agglomeration. Two band gap values of 1.89 and 2.40 eV were observed; these were assigned to the  $\text{O}^{2-}$ - $\text{Co}^{2+}$  and to  $\text{O}^{2-}$ - $\text{Co}^{3+}$  charge transfer processes, respectively, and the emission peaks for the  $\text{Co}_3\text{O}_4$ -NPs were observed in the visible region of the spectrum. Five Raman active modes, specified as the  $\text{A}_{1g}$ ,  $\text{E}_g$  and  $3\text{F}_{2g}$  modes of vibrations, were observed with the space group “*Fd3m*”. Subsequently, the  $\text{Co}_3\text{O}_4$ -NPs were investigated for their superior catalytic activity in three applications, which include (i) photodegradation of textile dye effluents (TDE) collected from the dyeing industry, Tiruppur, Tamil Nadu, India, (ii) catalytic hydrogenation of nitro-aromatic pollutants, such as 4-nitrophenol and 4-nitroaniline, and (iii) antibacterial potential in biomedical applications. The mechanisms of all the applications were discussed in depth, and kinetic studies were carried out wherever applicable. Hence, our results prove that the catalyst employed in the present study shows high performance in diverse applications.

## Acknowledgements

The authors duly acknowledge the financial support rendered by Loyola College, Tamil Nadu, India through Loyola College-Times of India (Grant No. 2LCTOI14CHM003) Major Research Project scheme *vide* (Project code: 2LCTOI14CHM003, dated 25.11.2014); and the authors (RJ and HAA) also thank deanship of scientific research, King Saud University, funding through Vice deanship of scientific Research Chair.

## References

- X. Wang, W. Tian, T. Zhai, C. Zhi, Y. Bando and D. Golberg, *J. Mater. Chem.*, 2012, **22**, 23310–23326.
- M. Manickam, V. Ponnuswamy, C. Sankar and R. Suresh, *Optik*, 2016, **127**, 5278–5284.
- K. Kaviyarasu, E. Manikandan, P. Paulraj, S. B. Mohamed and J. Kennedy, *J. Alloys Compd.*, 2014, **593**, 67–70.
- K. Kaviyarasu, E. Manikandan, J. Kennedy and M. Maaza, *RSC Adv.*, 2015, **5**, 82421–82428.
- F. Fang, J. Kennedy, E. Manikandan, J. Futter and A. Markwitz, *Chem. Phys. Lett.*, 2012, **521**, 86–90.
- K. Kaviyarasu, E. Manikandan, J. Kennedy, M. Jayachandran, R. Ladchumananandasivam, U. Umbelino De Gomes and M. Maaza, *Ceram. Int.*, 2016, **42**, 8385–8394.
- J. Kennedy, P. P. Murmu, J. Leveneur, A. Markwitz and J. Futter, *Appl. Surf. Sci.*, 2016, **367**, 52–58.
- K. Kaviyarasu, E. Manikandan, J. Kennedy, M. Jayachandran and M. Maaza, *Adv. Mater. Lett.*, 2016, **7**, 684–696.
- L. F. Liotta, H. Wu, G. Pantaleo and A. M. Venezia, *Catal. Sci. Technol.*, 2013, **3**, 3085–3102.
- Z. Ma, *Curr. Catal.*, 2014, **3**, 15–26.
- J. M. Xu and J. P. Cheng, *J. Alloys Compd.*, 2016, **686**, 753–768.
- H. Singh, A. K. Sinha, M. N. Singh, P. Tiwari, D. M. Phase and S. K. Deb, *J. Phys. Chem. Solids*, 2014, **75**, 397–402.
- K. Kaviyarasu, E. Manikandan, Z. Y. Nuru and M. Maaza, *Mater. Lett.*, 2015, **160**, 61–63.
- K. Kaviyarasu and D. Premanand, *Int. J. Nanosci.*, 2013, **12**, 1350033.
- K. Kaviyarasu, D. Sajan, M. S. Selvakumar, S. Augustine Thomas and D. Prem Anand, *J. Phys. Chem. Solids*, 2012, **73**, 1396–1400.
- K. Kaviyarasu, X. Fuku, G. T. Mola, E. Manikandan, J. Kennedy and M. Maaza, *Mater. Lett.*, 2016, **183**, 351–354.
- C. Maria Magdalane, K. Kaviyarasu, J. Judith Vijaya, B. Siddhardha and B. Jeyaraj, *J. Photochem. Photobiol., B*, 2016, **163**, 77–86.
- K. Kasinathan, J. Kennedy, M. Elayaperumal, M. Henini and M. Malik, *Sci. Rep.*, 2016, **6**, 38064.
- N. J. Sarathi, R. Karthik, S. Logesh, K. S. Rao and K. Vijayanand, 2nd International Conference on Environmental Science and Development IPCBEE, IACSIT Press, Singapore, 4, 2011.
- P. Suresh, J. J. Vijaya and L. J. Kennedy, *React. Kinet., Mech. Catal.*, 2015, **114**, 767–780.
- P. Suresh, J. J. Vijaya and L. J. Kennedy, *Mater. Sci. Semicond. Process.*, 2014, **27**, 482–493.
- C. O’Neil, F. R. Hawkes, D. I. Hawkes, N. D. Lourenço, H. M. Pinheiro and W. Delée, *J. Chem. Technol. Biotechnol.*, 1999, **74**, 1009–1018.
- Y. M. Slokar and M. A. M. Le, *Dyes Pigm.*, 1998, **37**, 33–56.
- J. J. Pignatello, E. Oliveros and A. Mackay, *Crit. Rev. Environ. Sci. Technol.*, 2006, **36**, 1–84.
- M. S. Lucas and J. A. Peres, *Dyes Pigm.*, 2006, **71**, 236–244.
- A. Alinsafi, F. Evenou, E. M. Adbulkarim, M. N. Pons, O. Benhammou and A. Yaacoubi, *Dyes Pigm.*, 2007, **74**, 439–445.
- M. Muruganandham and M. Swaminathan, *Sep. Purif. Technol.*, 2006, **48**, 297–303.
- K. Kaviyarasu, L. Kotsedi, A. Simo, X. Fuku, G. T. Mola, J. Kennedy and M. Maaza, *Appl. Surf. Sci.*, 2016, DOI: 10.1016/j.apsusc.2016.11.149.
- K. Kaviyarasu, A. Ayeshamariam, E. Manikandan, J. Kennedy, R. Ladchumananandasivam, U. U. Gomes, M. Jayachandran and M. Maaza, *Mater. Sci. Eng., B*, 2016, **210**, 1–9.



- 30 B. M. Mogudi, P. Ncube and R. Meijboom, *Appl. Catal., B*, 2016, **198**, 74–82.
- 31 A. Fedorczyk, J. Ratajczak, O. Kuzmych and M. Skompska, *J. Solid State Electrochem.*, 2015, **19**, 2849–2858.
- 32 K. Anand, R. M. Gengan, A. Phulukdaree and A. Chuturgoon, *J. Ind. Eng. Chem.*, 2015, **21**, 1105–1111.
- 33 S. K. Jesudoss, J. J. Vijaya, L. J. Kennedy, P. I. Rajan, H. A. Al-Lohedan, R. J. Ramalingam, K. Kaviyarasu and M. Bououdina, *J. Photochem. Photobiol., B*, 2016, **165**, 121–132.
- 34 Z. P. Xu and H. C. Zeng, *Chem. Mater.*, 2000, **12**, 3459–3465.
- 35 M. Mansournia and N. Rakhshan, *J. Mol. Struct.*, 2016, **1125**, 714–720.
- 36 A. Diallo, A. C. Beye, T. B. Doyle, E. Park and M. Maaza, *Green Chem. Lett. Rev.*, 2015, **8**, 30–36.
- 37 C. R. Dhas, R. Venkatesh, K. Jothivenkatachalam, A. Nithya, B. S. Benjamin, A. M. E. Raj, K. Jeyadheepan and C. Sanjeeviraja, *Ceram. Int.*, 2015, **41**, 9301–9313.
- 38 V. D. Mote, Y. Purushotham and B. N. Dole, *Ceramica*, 2013, **59**, 614–619.
- 39 X. Xia, J. Tu, X. Wang, C. Gu and X. Zhao, *Chem. Commun.*, 2011, **47**, 5786–5788.
- 40 Q. Liu, J. Tian, W. Cui, P. Jiang, N. Cheng, A. M. Asiri and X. Sun, *Angew. Chem., Int. Ed.*, 2014, **53**, 1–6.
- 41 S. Farhadi, K. Pourzare and S. Sadeghinejad, *J. Nanostruct. Chem.*, 2013, **3**, 16.
- 42 M. Ghiasi, A. Malekzadeh and H. Mardani, *Mater. Sci. Semicond. Process.*, 2016, **42**, 311–318.
- 43 S. Ardizzone, G. Spinolo and S. Trasatti, *Electrochimico. Am.*, 1995, **40**, 2683–2686.
- 44 P. Suresh, J. J. Vijaya, T. Balasubramaniam and L. J. Kennedy, *Desalin. Water Treat.*, 2014, **57**, 1–16.
- 45 K. Kaviyarasu, A. Mariappan, K. Neyvasagam, A. Ayeshamariam, P. Pandi, R. Rajeshwara Palanichamy, C. Gopinathan, G. T. Mola and M. Maaza, *Surf. Interfaces*, 2017, **6**, 247–255.
- 46 K. Kaviyarasu, N. Geetha, K. Kanimozhi, C. Maria Magdalane, S. Sivaranjani, A. Ayeshamariam, J. Kennedy and M. Maaza, *Mater. Sci. Eng., C*, 2017, **74**, 325–333.
- 47 P. K. Stoimenov, R. L. Klinger, G. L. Marchin and K. J. Klabunde, *Langmuir*, 2002, **18**, 6679–6686.
- 48 T. Hamouda and J. R. Baker, *J. Appl. Microbiol.*, 2000, **89**, 397–403.
- 49 I. Sondi and B. S. Sondi, *J. Colloid Interface Sci.*, 2004, **275**, 177–182.
- 50 N. M. Basith, J. J. Vijaya, L. J. Kennedy, M. Bououdina, S. Jenefar and V. Kaviyarasu, *J. Mater. Sci. Technol.*, 2014, **30**, 1108–1117.